Supplementary Materials for

Correlated Gene Expression Supports Synchronous Activity in Brain Networks

Jonas Richiardi*, Andre Altmann, Anna-Clare Milazzo, Catie Chang, M. Mallar Chakravarty, Tobias Banaschewski, Gareth J. Barker, Arun L.W. Bokde, Uli Bromberg, Christian Büchel, Patricia Conrod, Mira Fauth-Bühler, Herta Flor, Vincent Frouin, Jürgen Gallinat, Hugh Garavan, Penny Gowland, Andreas Heinz, Hervé Lemaître, Karl F. Mann, Jean-Luc Martinot, Frauke Nees, Tomáš Paus, Zdenka Pausova, Marcella Rietschel, Trevor W. Robbins, Michael N. Smolka, Rainer Spanagel, Andreas Ströhle, Gunter Schumann, Mike Hawrylycz, Jean-Baptiste Poline, Michael D. Greicius*, and the IMAGEN consortium (www.imagen-europe.com)

*Correspondence to: greicius@stanford.edu, jonas.richiardi@unige.ch

This PDF file includes:

Other Supplementary Materials for this manuscript includes the following:

Data Files S1 to S3 as files: AIBS_sample_details.xlsx, AIBS_probe_details.xlsx, IMAGEN_subject_identifiers.txt

1 Materials and methods

MRI Data overview and acquisition

The imaging data defining the functional networks used in this work are from a previous study in our group(*9*). We only summarize the most important characteristics here.

The sample consists of 15 healthy subjects (8 females), all right-handed, median age 25 (range 18-29). Subjects were asked to lie down in the scanner, close their eyes, and let their mind wander without focusing on any one thing in particular, for the duration of 10 minutes. Subjects were verified to stay awake. The scanner was a 3T General Electric MR750, with an 8-channel head coil. Whole-brain coverage was used, with 3.4 x 3.4 x 4 mm voxel size, spiral acquisition, and a TR of 2 s.

MRI Data processing

Functional images were motion-corrected, normalized to MNI space, interpolated to 2 mm isotropic voxels, and smoothed at 6 mm FWHM using SPM5 (http://www.fil.ion.ucl.ac.uk/spm/). The data were then high-pass filtered above 0.008 Hz, and physiological noise (heart rate and respiration rate) was removed from the data using RETROICOR and RVHRCOR(*29*).

MRI Data Independent component analysis

FSL MELODIC (http://www.fmrib.ox.ac.uk/fsl/ melodic/index.html) was applied to the data to produce 30 components. Out of these, 14 were selected as being non-artifactual networks in accordance with previous studies. The components were each thresholded manually, with a more liberal statistical cut-off for subcortical spatial clusters ($z=3.80\pm0.40$, minimum number of voxels 15) than for cortical spatial clusters ($z=7.0\pm0.47$). This resulted in 14 non-overlapping networks, which are consistently found in most subjects and studies on resting state(*1*, *11*, *30*, *31*), although the nomenclature may vary. These were auditory, basal ganglia, dorsal default-mode, high visual, language, left and right executive control, posterior salience, precuneus, primary visual, salience, sensorimotor, ventral default-mode network, and visuospatial (Figure S1). Each network and the rest of the cortex and subcortical areas were then subparcellated into a total of 499 regions of interest using a Ward clustering procedure(*32*).

Mapping Allen Institute biological samples to functional networks

Functional networks are defined in Montreal Neurological Institute (MNI) space, using the ICBM152 template. Allen Institute brains underwent structural MRI before dissection, and were normalized to MNI space. Therefore, MNI coordinates are available for all samples.

The 13 functional networks are non-overlapping, so samples can be mapped unequivocally. To account for possible small normalization errors and rounding errors in coordinate computations, if no one-to-one match is found, we expand the search to a 26-connected neighborhood around the sample's coordinate (i.e., including voxels that are within ± 1 voxel of either x, y, or z coordinates). Then, our mask of interest defining functional networks includes all Allen Institute samples whose MNI coordinates overlap with any of our 13 functional networks, or the 26-connected neighborhood. We excluded all samples that fell within the thalamus, midbrain, or pons because fMRI does not have the necessary spatial resolution to distinguish nuclei within these structures as defined in the AIBS data. We also excluded samples from the cerebellum and deep gray matter, in particular the hippocampus, to avoid biasing the analysis

due to possible differences in proportion of transcriptionally very diverse tissue in functional networks with respect to the rest of the brain. The final count of samples for each functional network is: dDMN: 84, Salience: 59, Sensorimotor: 47, Visuospatial: 51.

We also included AIBS samples that did not overlap with functional networks, again excluding thalamus, midbrain, pons, cerebellum, and deep gray matter, resulting in 1276 samples outside of functional networks.

Allen Institute data overview

The Allen Institute human microarray data (*10*) consists of brains from six subjects(*33*), of which two (brains 1 and 2 in Table S1) are full brains, and four are left hemispheres. The main demographic characteristics are summarized in Table S1.

The data were downloaded from the Allen Institute web site on May 7, 2013, thus benefitting from the improved within-batch and cross-batch array normalization procedures put in place in March 2013(*34*). The platform was an Agilent 4x44 Whole Human Genome array with an additional 16000 custom probes.

Allen Institute data probe reannotation

The assignment of probe sequences to genes was reannotated to the reference genome assembly hg19 (UCSC Genome Browser) (*35*), using Re-annotator (http://sourceforge.net/projects/reannotator/). If more than 2 mismatches between probe and reference sequence were found, the probe was instead matched to the whole genome. The type of hit (exonic or intronic) was recorded for further use in probe selection.

Allen Institute data probe normalization

Using all samples, we normalized each probe's expression level in turn by regressing out brain identifier and batch identifier. Due to the small number of subjects, average intensity, sex, age at death, and post-mortem interval have a very discrete set of values, and the statistical model fit is no better than the one we use here.

Allen Institute data probe selection and collapsing

We removed genes that do not have an Entrez ID. We also removed probes that are not called in any of the samples, where call information is provided in the Allen Institute data.

If genes were sampled by single probe, this probe was selected as long there was no sequence mismatch with the gene sequence, and it was aligned to the gene’s exon sequence. If there were several probes sampling the same gene, probe collapsing was conducted as follows: the probe with the fewest sequence mismatches was selected, as long as it matched to the exonic region, otherwise no probe was selected. Ties between probes having the same number of mismatches (or none) were broken by selecting the one with the highest standard deviation over samples, as a proxy for maximum information entropy.

Computing correlated gene expression networks

In mouse brains, correlated gene expression (called *correlation mode* in the anatomic gene expression atlas at http://mouse.brain-map.org/agea) shows that high similarity of gene expression is found within brain structures, and low similarity is found across brain structures(*15*).

In our case of interest, we aimed to measure correlated gene expression across 1777 samples, each represented by a 16,906-dimensional vector. The data will then be represented as a graph with a 1777x1777 adjacency matrix, where nodes correspond to samples, and edges encode the strength of the relationship between samples, with larger values corresponding to more similar gene expression. Several methods can be used to measure similarity of samples, and give a label (weight) to graph edges. Here, we used the Pearson product-moment correlation.

We also checked results using Spearman rank correlation. The edge weights of the correlated gene expression network were highly similar between Pearson and Spearman correlations ($\rho=0.961$, $p<10^{-15}$; Mantel test p-value=9×10^{-4} (1000 permutations)).

Test statistic and procedure for the relationship between functional networks and correlated gene expression

The aim of the testing procedure is to find out whether grouping gene expression samples according to their spatial overlap with functional networks gives rise to a "module-like" (or "community-like") subgraph in the statistical sense, that is, where the correlated gene expression is larger within the functional network, relative to the rest of the brain, than expected by chance. Both a test statistic and a testing procedure have to be defined. As explained in the main text, the chosen test statistic was the strength fraction. We note that many other metrics could be used, such as conductance, normalized cut, or a variant of out-degree fraction. We desired a metric that directly represents the ratio between within-network and out-of-network correlated gene expression (Figure S2), and that yields a higher number for a more "module-like" subgraph. Another approach would have been to use a modularity-based technique. Our rationale for avoiding this is twofold. First, results would hinge critically on the choice of a null model. Recent work has shown that generic null models (such as the configuration null model) are inappropriate for correlation networks(*36*) (where edges weights are given by Pearson correlation). Second, in a large-scale test of subgraph scoring functions(*37*), it has been found that scoring function combining internal and external connectivity, as is the case for the one we use here, had excellent performance for a wide variety of datasets. Finally, note that to keep the measure as simple as possible, we used the total strength, rather than the average strength, meaning that the strength fraction value is not directly comparable between functional networks because it depends on the size (number of vertices) of the functional network. However, this does not impact the statistical test value.

The permutation procedure is conducted to test how likely it is to observe a particular strength fraction value by chance in a subgraph of the same size. It is performed by permuting samples (over the full graph) irrespective of their assignment to a subgraph, to yield a null distribution. To account for clustering by subjects, samples are only permuted within subjects, not across subjects (clustered permutation). Here, a subgraph corresponded directly to one of the four functional networks of interest, and we used 10,000 permutations to assess significance.

While functional networks are distributed spatially, meaning they cross over different tissue types, and that their sample can be spatially distant, it is important to ensure that a high strength fraction does not simply reflect the fact that tissues are the same. For example, as noted, gene

expression in cerebellar samples is remarkably similar. To prevent any biases originating from this fact, we grouped samples into 88 tissue classes by their anatomical description, foregoing laterality (see Table S4). Then, we removed edges of the correlated gene expression graph corresponding to similarities between the same tissue classes (Figure S3 shows the location of edges that are removed).

Statistics on agreement of gene rankings between two brain subgroups

We split brains into two subgroups of three brains. In each subgroup, we multiplied one gene's expression level by 10, keeping all other expression levels at their original values, computed the strength fraction, and moved on to the next gene. This yielded two ordered lists of genes, after which we computed the probability of obtaining a certain overlap between the two ordered lists by chance. Using the list-intersection discovery test(*19*), we computed the p-value for the overlap between the two ranked lists at a False Discovery Rate of 5%. We give an example of the computation with the two brain subgroups as ([1 4 6], [2 3 5]).

Here, the total number of genes T is 16,906. The overlap size s between the two lists at a top-rank cutoff r of 370 (corresponding to 5% FDR, see below) is 162. A gene has a probability of ranking among the top r of $P^0 = \frac{r}{T} \cong 0.02$ in any of the two lists. Accordingly, the probability that a gene is listed in the top r in 2 or more lists is given by the binomial cumulative distribution function

$$P_2^0 = 1 - \sum_{\{i=0\}}^{1} \binom{1}{i} {P^0}^i (1 - P^0)^{1-i} I_{(0,1)}(i) \cong 5{\times}10^{-4}.$$

The number of genes overlapping by chance in 2 or more lists is approximately Poisson distributed, with mean $E = TP_2^0 \cong 8$. Under the null hypothesis, the probability of observing an overlap of size s is given by the Poisson cumulative distribution function

$$p_{h0} = 1 - e^{-E} \sum_{i=0}^{\lfloor s-1 \rfloor} \frac{E^i}{i!} < 10^{-15}$$

Lastly, we compute the False Discovery Rate, equal to the expectation on the proportion of false hits in all the significant tests, as

$$p_{FDR} = \frac{E}{s} \cong 0.05.$$

Generating the consensus list for all subgroups

We obtained all possible splits of the division of six brains into two subgroups, while keeping a full brain (either brain 1 or brain 2, see Table S1) in each subgroup, in order to balance the sample sizes. The six possible grouping permutations are ([1 4 6], [2 3 5]), ([1 3 4], [2 5 6]), ([1 3 5], [2 4 6]), ([1 3 6], [2 4 5]), ([1 4 5], [2 3 6]), and ([1 5 6], [2 3 4]). In each permutation, we applied the same procedure as above and thresholded at an FDR of 0.05. The statistical thresholding in each grouping can be seen as setting a regularization parameter controlling the number of non-zero components in a 16,906-dimensional vector. This is equivalent to enforcing a slightly different L_1-norm in each of the permutations. Thus, to obtain a consensus, we used stability selection(*20*) across all six lists, whereby the final consensus list (Table S2) consists of genes that appear in the majority of consensus lists (four or more). Results did not vary substantially if a more stringent criterion (appearance in five out of six splits) was chosen.

Allen Institute data gene set analysis

We used DAVID 6.7(*24*) (http://david.abcc.ncifcrf.gov/) to perform over-representation analysis for Gene Ontology (GO) annotations in Biological Processes and Molecular Function,

using default settings except for selecting the "ALL" versions of the ontologies rather than the "FAT" versions (equivalent to the Wolf et al settings(*28*)). The "ALL" versions comprise all terms in the GO hierarchy (across levels), while the "FAT" version removes more general (higher level) terms. We supply our custom background set of 16,906 genes, and the software's variant of a one-tailed Fisher exact test(*38*) is used for enrichment analysis. The reported p-value is corrected using Benjamini-Hochberg FDR(*39*) (FDR_{BH}). The results, shown in Table S5, point largely towards cation channels.

We repeat over-representation analyses using Panther 9.0(*40*) (http://www.pantherdb.org), Overrepresentation Test release 20141219, with the same custom background set, and FDR_{BH}-adjusted p-values. The results, shown in Table S6, largely agree (however, no GO Cellular Component term is significant in this analysis) and again point towards cation channels playing an important role.

We also compare our results with a study of the genetic determinants of axonal connectivity in the rodent brain(*28*). We use the available supplementary "table S5" (obtained by these authors using DAVID), and consider only annotation terms with an uncorrected p-value smaller than 0.05. We run our DAVID analysis using the same settings as the authors. Using our own results thresholded at an uncorrected significance level of 0.05, we compute the overlap in annotation terms, disregarding the data source (not provided in that supplementary "table S5"(*28*)). Using their data for "outgoing" axonal connectivity (268 unique annotation terms), we obtain an overlap of 50 unique terms with our results. Using their data for "incoming" axonal connectivity (194 unique annotation terms), we obtain an overlap of 34 unique terms. The terms are reported in Tables S7, S8.

We also looked for disease associations using Ingenuity Pathway Analysis. Here, a set of 6 genes in the list (CALB1, CDK1, NGFR, PTGS1, SCN1B, TSHZ3) is significantly overrepresented for Alzheimer's disease ($p<0.04$ FDR_{BH}). Another set of 6 genes is overrepresented for schizophrenia ($p<0.04$ FDR_{BH}). The full list of the 9 significant annotations is provided in Table S10.

Finally, we also attempted an initial description of the types of cells that may be driving our results. Here, we used the transcriptome database from Cahoy et al.(*25*) to examine whether some genes in our list are significantly overexpressing in some cell types. We converted mouse genes to humans orthologs using the HGNC Comparison of Orthology Predictions (HCOP) tool(*41*) (http://www.genenames.org/help/hcop). Then we compared our gene list with the Cahoy list, and counted when each gene had a significant overexpression in astrocytes, oligendendrocytes, and/or neurons.

IMAGEN data overview

The data was collected and processed by the IMAGEN consortium(*21*). Resting-state data was acquired at the end of the second MR session, with instructions to keep eyes closed, relax, and not sleep. All participants' parents gave written informed consent after information on the research procedures, and adolescents gave their assent after written information. INSERM is the legal promoter for French participants.

Here, we used 259 14-year old subjects (133 females) for which all three of functional MRI data, a structural T1-weighted image, and genetic data is available. This is a subset of the 385 IMAGEN subjects for which resting-state data was available: we excluded some subjects due to head motion larger than 3 mm in any direction (N = 74), failed co-registration (N = 16), or not having genotype data (N = 16), leading to an intermediary sample size of N = 279. The final

analysis removes a further N = 20 because they are genetically related (see *IMAGEN validation procedure* below). The functional images consist of a 6.5 mins echo-planar imaging resting-state scan with TR/TE/Flip Angle = 2200 ms / 30 ms / 75°, 64x64x40 voxels with 2.4 mm slice thickness and 1 mm slice gap and a field of view of 218x218mm, yielding isotopic 3.4mm voxels. The structural image consists of a T1-weighted MPRAGE image of 256x256x160/166 voxels (depending on manufacturer), with a 1.1 mm isotropic voxel size. Other parameters were based on the ADNI protocol (see http://adni.loni.usc.edu/methods/documents/mri-protocols/); full details are provided in the IMAGEN paper(*21*).

Genotype is measured from blood samples, using IlluminaQuad660 chip measuring 550K single nucleotide polymorphisms (SNPs).

IMAGEN MRI data processing

Functional and structural images were processed using FSL(*42*). Registration to MNI standard space was accomplished by first aligning functional scans to the structural image, and then normalizing them to MNI space using FLIRT(*43*). A 6mm smoothing kernel and a 6^{th} order Butterworth band pass filter (0.01-0.1 Hz) were applied to the fMRI data. Several sources of noise were regressed out: six movement parameters estimated by MCFLIRT, global signal, and time series from regions-of-interest (ROIs) in the ventricles, the white matter, and outside the brain. The same parcellation as for Allen Institute data was used. The mean time series was extracted from each of the 499 regions. Pearson correlations were computed between all pairs of regions. The matrix was then thresholded at 0, and the diagonal set to 0 to make it a valid adjacency matrix for an undirected, weighted graph with no self-loops. Further, connection strengths to ROIs not belonging to any of the 14 functional networks (N=357) were set to 0.

The strength fraction in the four functional networks of interest (dDMN, salience, sensorimotor, visuospatial) was computed for each subject, in the same manner as described in the section on Allen Institute gene expression data.

IMAGEN genetic data processing

Data on a total of 557,124 SNPs were provided by IMAGEN. These were filtered for minor allele frequency (<5%), genotyping rate (<95%), and Hardy-Weinberg-Equilibrium (P<6e-7), resulting in a final set of 492,856 SNPs.

IMAGEN validation procedure

With PLINK(*44*), we used strength fraction as a quantitative trait in an additive genetic model corrected for sex, scanning site, population structure (5 PCA components), and motion covariates (translation: max and mean of x,y,z, as well as RMS; rotation: max and mean of roll, pitch, yaw; framewise displacement (FD, defined either by Van Dijk(*45*) or Power(*46*)): Van Dijk and Power means, percentage Power FD at 0.02 and 0.05, total Power FD, total translations in x,y,z, total rotations in pitch, roll, yaw). A genetic relationship matrix (GRM) was computed for all 279 subjects using the GCTA software(*47*). Based on the GRM 20 subjects were removed due to relatedness as indicated by a relationship score in the GRM of 0.025 or more, leading to a final sample size of 259. The genome-wide association analysis yielded approximately 490K p-values, one per SNP, on the null hypothesis of no association between genotype and strength fraction in functional networks. There was no sign for inflation of p-values as the genomic inflation factor was close to 1.0 (λ=1.00803; Figure S5). The most significant SNP was rs9870687 with a P-value of 6.57×10^{-6}. Thus, no SNP survived the Bonferroni corrected threshold of 1.01×10^{-7} (Figure S5).

Our main interest is to verify the enrichment of statistical association signals in the consensus list compared to the list of 16,906 background genes as well as the enrichment in the significant GO terms identified by the previous overrepresentation analysis (Table S5). For computing the enrichment scores for the 7 GO terms we use recent developments in pathway analysis for GWAS data(*48*), in particular the z-statistic method(*49*) implemented in GSA-SNP(*22*), where in order to test all 7 GO terms we removed the software's default limit to test only gene sets with sizes 10 to 200 genes. Briefly, every gene's p-value is taken from its second-ranked SNP within the region of transcription start site to transcription end including the 10Kb upstream and downstream, respectively. This approach has been shown to reduce the impact of randomly highly significant top SNPs(*50*). The z-statistic is then computed on the basis of all p-values without the requirement to set an arbitrary cut-off. More precisely, p-values are converted to scores using the $-\log_{10}$ transformation, μ and σ are the mean and standard deviation, respectively, of the gene scores on the set of all genes. S and n are respectively the mean gene score and the size of gene set to be tested. The z-statistic is then computed as $Z=(S - \mu)/(\sigma * n^{-0.5})$. All but one GO terms were significantly enriched in this analysis (Z-scores and p-values for all 7 GO terms are listed in Table S9). The non-significant term is *extracellular region*.

GSA-SNP does not allow for selecting a reduced background set of genes. Therefore, we compute the Z-statistic for the consensus list manually using μ_{back} and σ_{back} (instead of μ and σ) corresponding to mean and standard deviation of the gene scores in our background list. The consensus list showed significant enrichment (Z = 2.55; P=0.006) with respect to the background list and, which was even more pronounced with respect to all genes ($Z = 3.76$; $P = 8.38 \times 10^{-5}$).P-values were confirmed using a non-parametric permutation test with 10,000 permutations by selecting random gene sets of equivalent size from either the background set (P = 0.0059) or the full list of genes ($P < 4 \times 10^{-4}$).

In order to capture the multiallelic effect of the consensus list for visualization purposes (Figures 2, S5), we computed an individual post-hoc multilocus genetic score as follows: the score is based on 136 SNPs (i.e., one SNP per gene in the list) and represents the sum of the number of minor alleles for all those SNPs, weighted by the direction of the effect on the strength fraction (SF) phenotype (with '1' in case the minor allele increases the SF and with '-1' in case the minor allele decreases the SF), and divided by the number of nonmissing SNPs. The SNPs used for computing the genetic score were the same ones used for computing the Z-

statistic, i.e., the 2nd most significant SNP per gene was selected. This scoring scheme is similar to the one performed by Heck et al(*27*); the only difference being that we use all SNPs instead of only the nominally significant SNPs.

Allen Institute Mouse Gene expression data overview

Allen Institute Mouse Gene expression data consist of whole-brain In Situ Hybridization (ISH) data that have been obtained from 24 μm sections of 56-day old C57BL/6J mice. Two section datasets are available: the coronal dataset, which covers 4,376 genes, and the sagittal dataset which covers more than 20,000 genes (*15*, *51*). The data from all experiments are coregistered to the common Allen Brain Atlas template, and expression values are available in 200 μm^3 voxels. Here, we use the coronal dataset, which has better spatial coverage and registration(*15*), but fewer genes, and corresponds to the sections used for the connectivity data and model (see below). We use expression density (sum of expressing pixels / sum of all pixels in division).

We obtained a list of genes and related information using the following API call:

`http://api.brain-map.org/api/v2/data/Gene/query.json?criteria=products[id$eq1]&only=id,acronym,entrez_id,homologene_id&num_rows=all&order=id`

We obtained a list of meta-data for all 1205 brain structures as follows:

`http://api.brain-map.org/api/v2/data/Structure/query.json?criteria=[graph_id$eq1]&include=structure_centers&num_rows=all&order=id`

We obtained the SectionDatasets (ISH images), omitting failed experiments, as follows:

`http://api.brain-map.org/api/v2/data/SectionDataSet/query.json?criteria=[failed$eqfalse][expression$eqtrue],products[id$eq1],plane_of_section[id$eq1]&include=genes&num_rows=all&order=id`

Finally, we mapped the SectionDatasets into brain structures by running the structure unionizer over each SectionDataset in turn (example here with dataset 32386, and we only included only a few structure_ids for brevity):

```
http://api.brain-map.org/api/v2/data/StructureUnionize/query.json?criteria=[section_data_set_id$eq32386][structure_id$in1,2,…,182305713]&only=structure_id,expression_energy,expression_density&num_rows=all
```

Allen Institute Mouse Gene expression data processing

We transformed the dataset into an nStructures x nGenes matrix of expression values, excluding structures where no genes are expressed (according to automated expression detection), and genes that are not expressed in any structure (likewise), yielding a 'raw' 844 x 3191 matrix. We normalize each gene's expression value across tissues by fitting a constant model ($\mathbf{y}=\beta x \mathbf{1}$), and used the prediction residual as that gene's normalized expression value.

Allen Institute Mouse connectivity data overview

The Allen Mouse Brain Connectivity Atlas (AMBCA)(*23*) is based on viral tracing of axonal projections in coronal mouse brain sections. It consists of both an ipsilateral and a

contralateral connectivity matrix between 295 brain regions. An optimization and regression model then yields connection weights between 213 'meso-scale' regions. Here, to help correspondence with our human gene expression data where we used only cortical samples, we focus on the 38 regions of the mouse isocortex.

We obtained the model connection weights and their corresponding p-values from supplementary table 3 of(*23*), for both ipsilateral and contralateral connectivity. Note that this connectivity matrix **M** is not symmetric.

Allen Institute Mouse connectivity data processing

Here, we use the ipsilateral connectivity matrix, but results hold when using the contralateral connectivity matrix (see main text). First, we correct the p-values of the connectivity model for multiple comparisons using the FDR procedure. Then, for each pair of regions, we want to test the hypothesis that either there is a connection between region 1 and region 2, or there is a connection between region 2 and region 1. This is to reflect the fact that functional connectivity is undirected, and we use axonal connectivity as a ground truth of what functional connectivity relies on. In order to combine the two p-values for each edge (1→2 and 2→1) into a single value, we use the Fisher (chi-square) product combination. We then obtain a symmetrized 38x38 adjacency matrix $\mathbf{B}=(\mathbf{M}+\mathbf{M}^{T})/2$, which we further normalize as $\mathbf{C}=\mathbf{S}^{-1/2}\mathbf{B}\mathbf{S}^{-1/2}$, where **S** is a diagonal matrix containing the strengths of each vertex in **B** (*52*, *53*). Other normalizations, such as used for spectral segmentation ($\mathbf{C}=\mathbf{S}^{-1}\mathbf{B}$) (*54*)are also possible and do not change the result of the statistical test used in the validation procedure.

Allen Institute Mouse validation procedure

Here, we wanted to test whether our consensus list of genes, derived in post-mortem humans and validated in-vivo in adolescents, was also significantly associated with axonal connectivity. We first obtained mouse orthologs for our human list of genes, using the HGNC Comparison of Orthology Predictions (HCOP) database (*41*) downloaded in September 2014. If more than one ortholog was found, we selected the one supported by the most databases (15th column in the '15-column' format of the HCOP bulk downloads tool). There were no ties. Out of 136 human genes in our list, 125 could be matched to mouse genes. Of these, 57 corresponded to non-empty ISH experiments in the Allen Mouse gene expression data. We compute a correlated gene expression network between the 38 isocortex regions using values of the 57 non-empty orthologs, yielding a 38x38 adjacency matrix **T** representing transcriptional similarity across the isocortex using our list of genes. Then, our test statistic was based on the non-parametric Mantel test (*55*) of association between **T** and **C**, which represents matrices as vectors (lexicographical rearrangement) and computes their correlation (Spearman in our case, but using Pearson here does not change the significance of our results). Because many edges were non-significant in **C**, we thresholded them out of both **T** and **C,** and removed these from the vector. Leaving zeros instead would yield artificial correlations between **T** and **C**. To generate the null distribution of the test statistic, instead of permuting rows and columns of one of the matrices, we picked 57 (non-empty) genes at random 10,000 times. This represents the strength of association between transcriptional similarity and axonal connectivity strength using random genes. The p-value is then obtained in the usual fashion for permutation tests.

2 Supplementary Text

Rationale for in-vivo validation

We wanted to validate whether genetic variation in the genes of the consensus list derived from post-mortem gene expression data will also show changes of in vivo rs-fMRI connectivity. While for the discovery of the genes in the consensus list our hypothesis was that similar gene expression levels equate with membership to certain functional networks, the hypothesis for this validation step is that genetic variation as measured by single nucleotide polymorphisms (SNPs) will alter the in vivo observed strength fraction in functional networks. Here genetic variation can act in multiple ways such as (i) presence of expression quantitative trait loci (eQTLs) that directly alter abundance of the associated gene's mRNA, (ii) non-synonymous SNPs that alter the amino acid sequence and therefore the resulting protein's physiochemical properties, (iii) variants influencing mRNA splicing, (iv) variants disrupting methylation sites within the gene regulatory region. Thus, many genetic variants alter either mRNA transcript abundance or the protein's efficiency, which in turn may be translated into increased or reduced mRNA transcript abundance.

3 Supplementary Figures

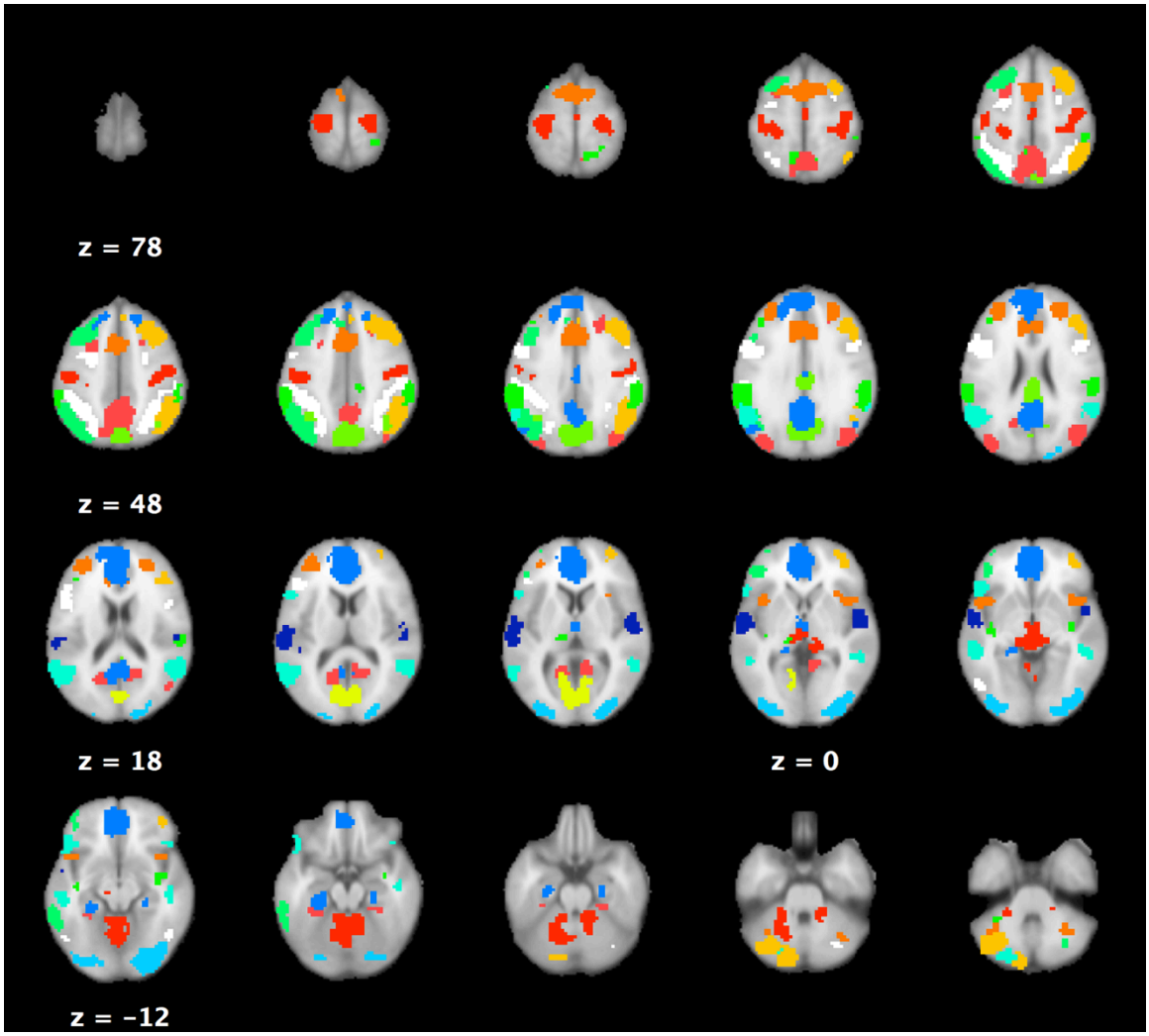

4 Fig S1.

13 resting-state functional networks. Axial view, normalized to an MNI template. The basal ganglia network is excluded from the analysis, and not shown here. Also, note that Allen Institute human microarray samples corresponding to parts of functional networks falling in the cerebellum are excluded from the analysis (only cortical samples are used).

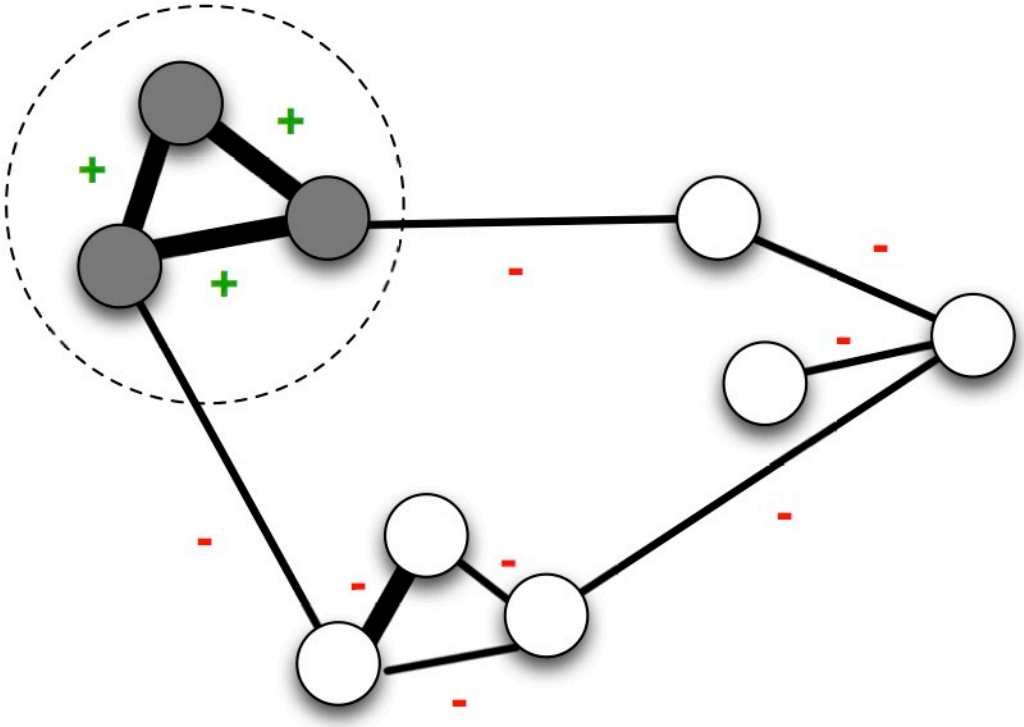

5 Fig. S2.

Principle for the strength fraction computation. The functional network of interest is shown with grey vertices and its outline by a dashed circle. All Edges labeled '+' go in the numerator of the strength fraction (W_i), while all edges labeled '-' go in the denominator (T-W). In this simple example, there is only one functional network, so $W=W_i$.

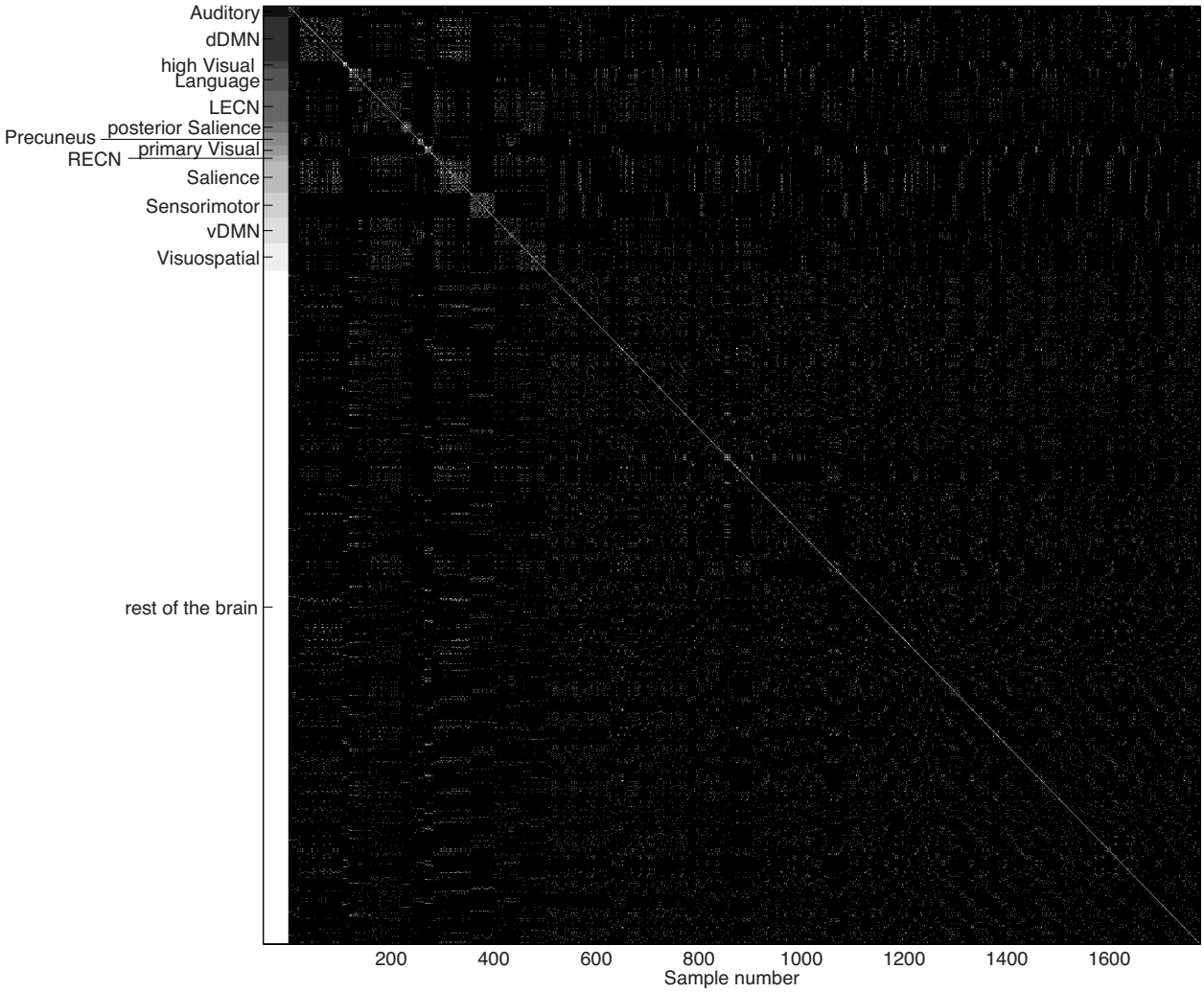

Fig. S3.

Tissue-tissue adjacency matrix. Edges labeled in white indicate that the corresponding samples are of the same tissue class. Sample grouping into 13 functional networks is indicated in the leftmost column. To account for correlation bias due to spatial proximity and being in the same tissue class, these edges are set to zero.

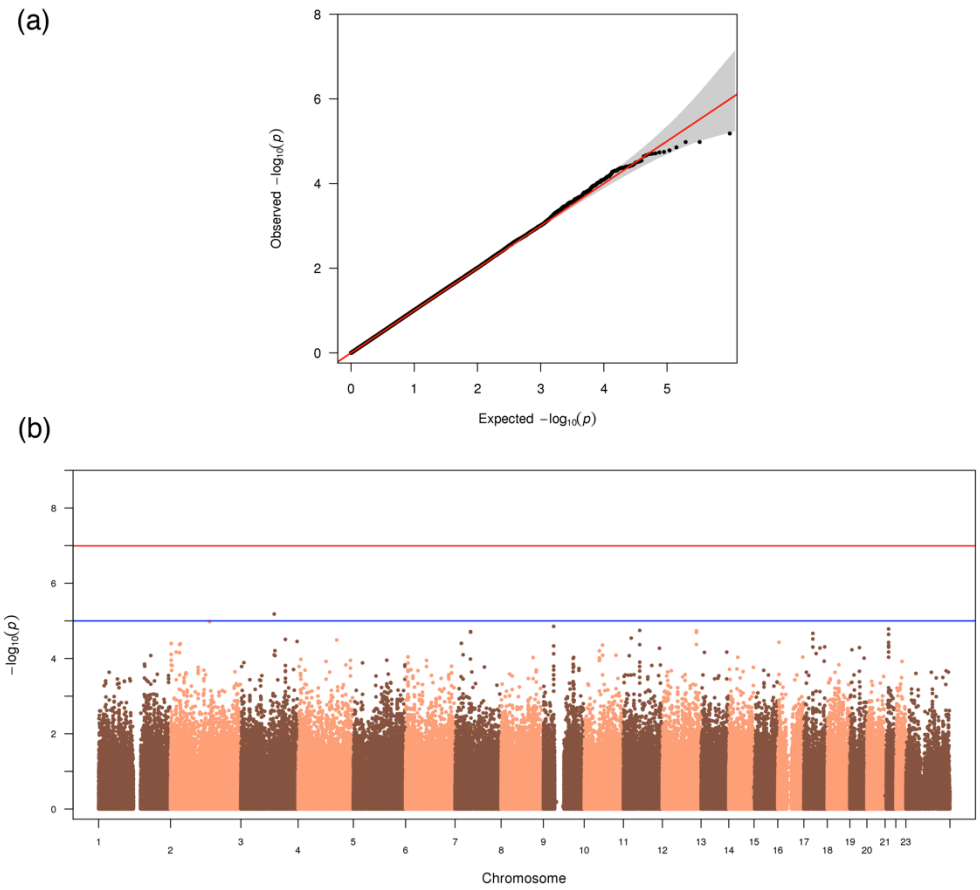

7 Fig. S4.

Genome-wide association study on IMAGEN data. (A) QQ plot, showing no p-value inflation. (B) Manhattan plot, showing no SNP surviving the Bonferroni-corrected level of significance (red line).

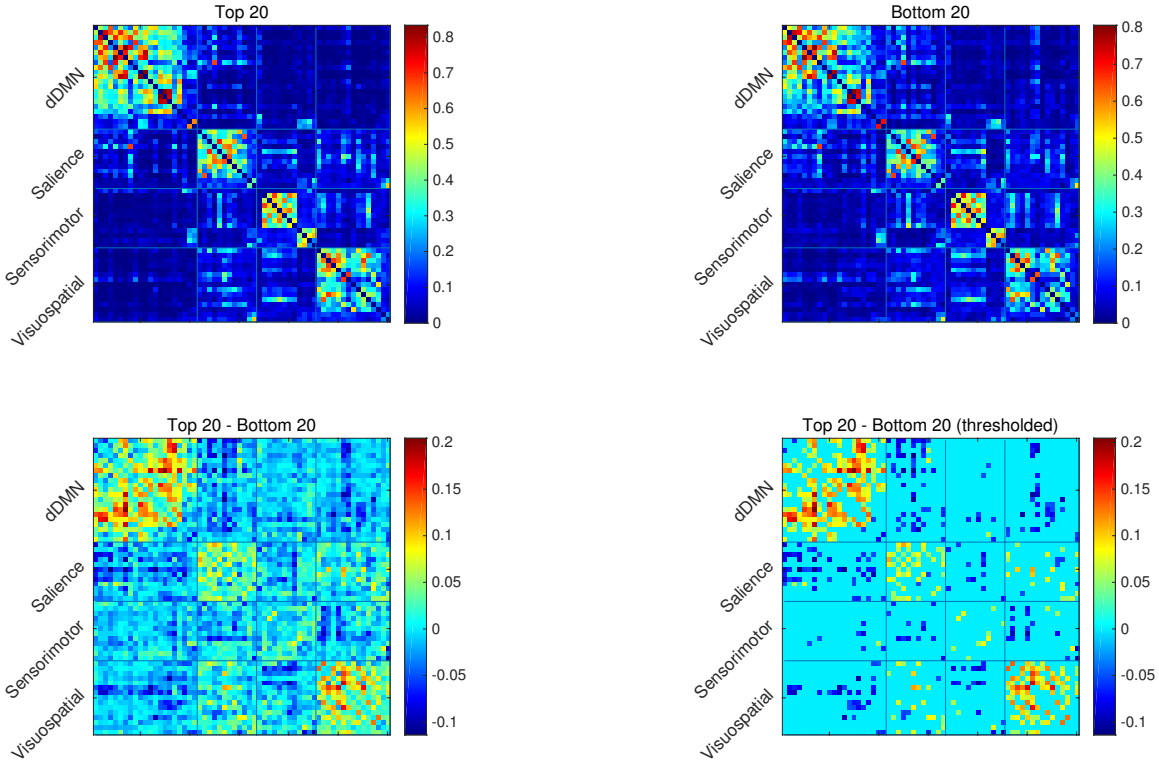

Fig. S5

Adjacency matrices for in-vivo functional connectivity differences related to our list of genes. (top row) Adjacency matrices of the in-vivo IMAGEN fMRI connectivity graph for average of top 20 or bottom 20 subjects, ranked by their multilocus genetic score. (bottom row) Difference of adjacency matrices, unthresholded (left) and thresholded (right). The thresholded version corresponds to Fig. 3 of the main manuscript.

9 Table S1.

Demographic information about the AIBS human microarray dataset. M: male, F: female, L: left, R: right

ID	Allen ID	Sex	Age [years]	Handedness	Hemispheres	Post-mortem interval [hours]
1	H0351.2001	M	24	left	L+R	23
2	H0351.2002	M	39	left	L+R	10
3	H0351.1009	M	57	mixed	L	25.5
4	H0351.1012	M	31	right	L	17.5
5	H0351.1015	F	49	right	L	30
6	H0351.1016	M	55	right	L	18

Table S2.

136 consensus genes linked to functional networks. The genes are grouped by the number of splits of AIBS data (into two groups of three subjects each) in which the gene is top-ranked. When known, genes related to ion channels are highlighted in bold, and genes related to neurotransmitters are highlighted in red (note that there are overlaps in function).

All splits (most stable)	ADAM23 ANKRD6 ATP6V1C2 BAIAP3 C3orf55 CARTPT CCDC39 CD70 CDK1 CNTN6 CRYBA2 CTXN3 CXXC11 DMRT3 EPN3 FEZF1 FZD7 GAL **GLRA3** GNA14 GNGT2 GRP HSD11B1 KANK4 **KCNA1 KCNA3 KCNA5 KCNC1 KCTD15** KRT1 KRT31 LAIR2 LINC00238 LMOD3 LRRC38 LYPLA2 MGP MYH7 MYLK3 NEB **NECAB2** NEFH NEUROD6 NGFR NOL4 NOV NRP1 ONECUT2 PCP4 PIRT PNMT PRR15 PRSS35 PTGS1 RBP4 RBPMS2 RHOBTB2 RSPH9 SCARA5 **SCN1B SCN4B** SEMA7A SHD SHISA9 SIX3-AS1 SLC16A6 SLC22A10 SLN SV2C SYT10 **SYT2** TDO2 TGFBI TINCR TLX2 TNNT2 TRIM29 TSHZ3	AMDHD1 ASGR2 CD163L1 COL5A2 CYP2C18 FAM163A **GABRA5** GALP GPR26 GPR88 GPX3 HPCAL1 IL13RA2 ISCU NEXN NKAIN4 NPBWR2 ONECUT3 OR51E2 PLCH1 **PVALB SNAP25** SPHKAP TMEM52 TSPAN8 ZCCHC18	**5/6 splits**
	ALOX12 CALB1 **CCBE1** CD6 CDR2L CPLX1 ENPP6 GMPR GOLT1A GPR20 HOXD1 HPCA IL33 IQCJ KLK1 KLK8 LGR6 LINC00617 MS4A8 MYBPC1 NUPR1L PYDC1 RTP1 SEMA3C SH3RF2 SLC16A5 SLC20A2 SLC39A12 SOST WISP1 WISP2 WNT4	**4/6 splits**

11 Table S3.

Subset of gene ontology annotations for genes of our consensus lists. CC: cellular component, MF: molecular function, ID: numeric identifier in Gene Ontology. Most specific subset of Gene ontology CC and MF terms where genes of our consensus list are significantly overrepresented ($p<0.05$ FDR_{BH}) in the DAVID analysis, and corresponding uncorrected p-value of these terms on IMAGEN dataset and Wolf et al's Rodent axonal connectivity data. For consistency, all p-values shown here are uncorrected.

Type	ID	Term	Allen	IMAGEN	Rodent(*28*)	
					afferent	efferent
MF	0022843	Voltage-gated cation channel activity	1.92E-04	1.17E-09	2.0E-03	<10E-15
CC	0034702	Ion channel complex	1.32E-04	2.64E-11	n/a	n/a
	003470	Potassium channel complex	4.95E-04	2.80E-05	n/a	n/a
	0008076	Voltage-gated potassium channel complex	4.95E-04	2.80E-05	5.4E-02	5.5E-02
	0005576	Extracellular region	7.87E-04	3.82E-01	3.6E-02	1.9E-02
	0005886	Plasma membrane	9.98E-04	4.00E-20	n/a	n/a
	003470	Cation channel complex	4.61E-04	8.66E-10	n/a	n/a

12 Table S4.

88 tissue classes derived from anatomical labels

Angular gyrus, inferior bank of gyrus
Angular gyrus, superior bank of gyrus
Anterior orbital gyrus
Cingulate gyrus, frontal part, inferior bank of gyrus
Cingulate gyrus, frontal part, superior bank of gyrus
Cingulate gyrus, parietal part, inferior bank of gyrus
Cingulate gyrus, parietal part, superior bank of gyrus
Cingulate gyrus, retrosplenial part, inferior bank of gyrus
Cingulate gyrus, retrosplenial part, superior bank of gyrus
Cuneus, peristriate
Cuneus, striate
Frontal operculum
Frontal pole, inferior aspect
Frontal pole, medial aspect
Frontal pole, superior aspect
Fusiform gyrus, bank of cos
Fusiform gyrus, bank of the its
Fusiform gyrus, lateral bank of gyrus
Gyrus rectus
Heschls gyrus
Inferior frontal gyrus, opercular part
Inferior frontal gyrus, orbital part
Inferior frontal gyrus, triangular part
Inferior occipital gyrus, inferior bank of gyrus
Inferior occipital gyrus, superior bank of gyrus
Inferior rostral gyrus
Inferior temporal gyrus, bank of mts
Inferior temporal gyrus, bank of the its
Inferior temporal gyrus, lateral bank of gyrus
Lateral orbital gyrus
Lingual gyrus, peristriate
Lingual gyrus, striate
Long Insular Gyri
Medial orbital gyrus
Middle frontal gyrus, inferior bank of gyrus
Middle frontal gyrus, superior bank of gyrus
Middle temporal gyrus, inferior bank of gyrus
Middle temporal gyrus, superior bank of gyrus
Occipital pole, inferior aspect
Occipital pole, lateral aspect
Occipital pole, superior aspect

Occipito-temporal gyrus, inferior bank of gyrus
Occipito-temporal gyrus, superior bank of gyrus
Paracentral lobule, anterior part
Paracentral lobule, anterior part, inferior bank of gyrus
Paracentral lobule, anterior part, superior bank of gyrus
Paracentral lobule, posterior part, bank of cingulate sulcus
Paracentral lobule, posterior part, lateral bank of gyrus
Parahippocampal gyrus, bank of the cos
Parahippocampal gyrus, lateral bank of gyrus
Paraterminal gyrus
Parolfactory gyri
Piriform cortex, left
Planum polare
Planum temporale
Postcentral gyrus, bank of the central sulcus
Postcentral gyrus, bank of the posterior central sulcus
Postcentral gyrus, inferior lateral aspect of gyrus
Postcentral gyrus, superior lateral aspect of gyrus
Posterior orbital gyrus
Precentral gyrus, bank of the central sulcus
Precentral gyrus, bank of the precentral sulcus
Precentral gyrus, inferior lateral aspect of gyrus
Precentral gyrus, superior lateral aspect of gyrus
Precuneus, inferior lateral bank of gyrus
Precuneus, superior lateral bank of gyrus
Precuneus, inferior lateral bank of gyrus
Precuneus, superior lateral bank of gyrus
Putamen
Short Insular Gyri
Subcallosal gyrus
Subcollosal gyrus
Superior frontal gyrus
Superior frontal gyrus, lateral bank of gyrus
Superior frontal gyrus, medial bank of gyrus
Superior occipital gyrus, inferior bank of gyrus
Superior occipital gyrus, superior bank of gyrus
Superior rostral gyrus
Superior temporal gyrus, inferior bank of gyrus
Superior temporal gyrus, lateral bank of gyrus
Supramarginal gyrus, inferior bank of gyrus
Supramarginal gyrus, superior bank of gyrus
Supraparietal lobule, inferior bank of gyrus
Supraparietal lobule, superior bank of gyrus
Temporal pole, inferior aspect
Temporal pole, medial aspect

Temporal pole, superior aspect
Transverse gyri

13 Table S5:

Gene Ontology Molecular Function (MF) and Cellular Component (CC) terms for which our consensus list of genes is significantly over-represented ($p < 0.05$ FDR_{BH}), obtained using DAVID.

Type	ID	term	p-value	FDR_{BH}
MF	0022843	Voltage-gated cation channel activity	1.92E-04	4.97E-02
CC	0034702	Ion channel complex	1.32E-04	2.11E-02
	003470	Potassium channel complex	4.95E-04	2.62E-02
	0008076	Voltage-gated potassium channel complex	4.95E-04	2.62E-02
	0005576	Extracellular region	7.87E-04	3.12E-02
	0005886	Plasma membrane	9.98E-04	3.16E-02
	003470	Cation channel complex	4.61E-04	3.64E-02

14 Table S6:

Gene Ontology Molecular Function and Biological Processes terms over-representation analysis results for our consensus list using Panther, showing terms where our genes are significantly over-represented ($p < 0.05$ FDR_{BH}-adjusted).

Type	Term	p-value (FDR_{BH})
MF	receptor activity	2.93E-02
	voltage-gated ion channel activity	2.93E-02
	transmembrane transporter activity	2.93E-02
	cation channel activity	2.93E-02
	transporter activity	2.93E-02
	voltage-gated potassium channel activity	2.93E-02
	nucleic acid binding	3.48E-02
BP	multicellular organismal process	< 10E-15
	single-multicellular organism process	< 10E-15
	system process	< 10E-15
	cell-cell signaling	< 10E-15
	neurological system process	< 10E-15
	cell communication	< 10E-15
	synaptic transmission	1.30E-03
	cellular process	1.30E-03
	developmental process	5.40E-03
	angiogenesis	5.40E-03
	mesoderm development	5.40E-03
	system development	5.40E-03
	cation transport	6.50E-03
	ion transport	6.60E-03
	transport	7.50E-03
	localization	1.15E-02
	sensory perception	1.17E-02
	muscle organ development	1.49E-02
	immune system process	2.71E-02
	neurotransmitter secretion	2.71E-02
	macrophage activation	2.71E-02
	receptor-mediated endocytosis	2.71E-02
	cell-cell adhesion	2.84E-02

Table S7: Overlap between our human microarray consensus gene list annotation terms and those for afferent (incoming) rodent neuronal connectivity. Terms listed here have uncorrected p-values < 0.05 in both our results and those of (*28*).

Anatomical structure development	Cation channel activity
Cell fraction	Cell part morphogenesis
Cell projection morphogenesis	Cell-cell signaling
Channel activity	Extracellular region
Gated channel activity	Glycoprotein
Ion channel activity	Ion transport
Ionic channel	Metal ion transmembrane transporter activity
Metal ion transport	Multicellular organismal development
Negative regulation of multicellular organismal process	Nervous system development
Neurogenesis	Neuropeptide signaling pathway
Passive transmembrane transporter activity	Potassium channel activity
Potassium channel, voltage dependent, kv, tetramerisation	Potassium ion transport
Regulation of multicellular organismal process	Signal
Substrate specific channel activity	Synapse
Synaptic transmission	Transmission of nerve impulse
Voltage-gated cation channel activity	Voltage-gated channel
Voltage-gated channel activity	Voltage-gated ion channel activity

Table S8 Overlap between our human microarray consensus gene list annotation terms and those for efferent (outgoing) rodent neuronal connectivity. Terms listed here have uncorrected p-values < 0.05 in both our results and those of (*28*)

alkali metal ion binding	anatomical structure development
cation channel activity	cation transmembrane transporter activity
cation transport	cell part morphogenesis
cell projection morphogenesis	cell-cell signaling
channel activity	extracellular region
extracellular region part	extracellular space
gated channel activity	glycoprotein
ion channel activity	ion transmembrane transporter activity
ion transport	ionic channel
metal ion transmembrane transporter activity	metal ion transport
monovalent inorganic cation transport	multicellular organismal development
negative regulation of multicellular organismal process	nervous system development
neurogenesis	neurotransmitter transport
organ morphogenesis	palmitate
passive transmembrane transporter activity	potassium
potassium channel activity	potassium channel, voltage dependent, kv, tetramerisation
potassium ion binding	potassium ion transport
regulation of multicellular organismal process	signal
substrate specific channel activity	substrate-specific transmembrane transporter activity
substrate-specific transporter activity	synapse
synaptic transmission	system development
transmembrane transporter activity	transmission of nerve impulse
transport	voltage-gated cation channel activity
voltage-gated channel	voltage-gated channel activity
voltage-gated ion channel activity	voltage-gated potassium channel activity

17 Table S9

Z-scores and P-values for Gene Ontology Molecular Function (MF) and Cellular Component (CC) terms, which were significant in the AIBS dataset using DAVID and in the independent validation on the IMAGEN dataset, obtained using GSA-SNP.

Type	ID	Term	Z-score	P-value
MF	0022843	Voltage-gated cation channel activity	5.97	1.17E-09
CC	0034702	Ion channel complex	6.56	2.64E-11
	003470	Potassium channel complex	4.03	2.80E-05
	0008076	Voltage-gated potassium channel complex	4.03	2.80E-05
	0005576	Extracellular region	0.30	3.82E-01
	0005886	Plasma membrane	9.11	4.00E-20
	003470	Cation channel complex	6.02	8.66E-10

18 Table S10

Significant disease annotations for our consensus list using Ingenuity Pathway Analysis ($p<0.05$ FDR_{BH}).

Annotation	**p-value (FDR_{BH})**
Huntington's Disease	3.10E-02
Alzheimer's disease	3.10E-02
Huntington disease grade 1 Huntington's disease	3.10E-02
Atrophy of motor axons	3.10E-02
Neurogenesis of neuronal progenitor cells	3.10E-02
Quantity of neurofilaments	3.10E-02
Schizophrenia	3.12E-02
Amyotrophic lateral sclerosis	3.64E-02
Formation of neurofilament inclusion	4.11E-02

19 IMAGEN consortium author list

Lisa Albrecht (Charité), Chris Andrew (IoP), Mercedes Arroyo (Cambridge University), Eric Artiges (INSERM), Semiha Aydin (PTB), Christine Bach (Central Institute of Mental Health), Tobias Banaschewski (Central Institute of Mental Health), Alexis Barbot (Commissariat à l'Energie Atomique), Gareth Barker (IoP), Nathalie Boddaert (INSERM), Arun Bokde (Trinity College Dublin), Zuleima Bricaud (INSERM), Uli Bromberg (University of Hamburg), Ruediger Bruehl (PTB), Christian Büchel (University of Hamburg), Arnaud Cachia (INSERM), Anna Cattrell (IoP), Patricia Conrod (IoP), Patrick Constant (PERTIMM), Jeffrey Dalley (Cambridge University), Benjamin Decideur (Commissariat à l'Energie Atomique), Sylvane Desrivieres (IoP), Tahmine Fadai (University of Hamburg), Herta Flor (Central Institute of Mental Health), Vincent Frouin (Commissariat à l'Energie Atomique), Jürgen Gallinat (Charité), Hugh Garavan (Trinity College Dublin), Fanny Gollier Briand (INSERM), Penny Gowland (University of Nottingham), Bert Heinrichs (Deutsches Referenzzentrum für Ethik), Andreas Heinz (Charité), Nadja Heym (University of Nottingham), Thomas Hübner (Technische Universität Dresden), James Ireland (Delosis), Bernd Ittermann (PTB), Tianye Jia (IoP), Mark Lathrop (CNG), Dirk Lanzerath (Deutsches Referenzzentrum für Ethik), Claire Lawrence (U Nottingham), Hervé Lemaitre (INSERM), Katharina Lüdemann (Charité), Christine Macare (IoP), Catherine Mallik (IoP), Jean-François Mangin (INSERM), Karl Mann (Central Institute of Mental Health), Jean-Luc Martinot (INSERM), Eva Mennigen (Technische Universität Dresden), Fabiana Mesquita de Carvahlo (IoP), Xavier Mignon (PERTIMM), Ruben Miranda (INSERM), Kathrin Müller (Technische Universität Dresden), Frauke Nees (Central Institute of Mental Health), Charlotte Nymberg (IoP), Marie-Laure Paillere (INSERM), Tomas Paus (University of Toronto), Zdenka Pausova (University of Toronto), Jean-Baptiste Poline (Commissariat à l'Energie Atomique), Luise Poustka (Central Institute of Mental Health), Michael Rapp (Charité), Gabriel Robert (IoP), Jan Reuter (Charité), Marcella Rietschel (Central Institute of Mental Health), Stephan Ripke (Technische Universität Dresden), Trevor Robbins (Cambridge University), Sarah Rodehacke (Technische Universität Dresden), John Rogers (Delosis), Alexander Romanowski (Charité), Barbara Ruggeri (IoP), Christine Schmäl (Central Institute of Mental Health), Dirk Schmidt (Technische Universität Dresden), Sophia Schneider (University of Hamburg), MarkGunter Schumann (IoP), Florian Schubert (PTB), Yannick Schwartz (Commissariat à l'Energie Atomique), Michael Smolka (Technische Universität Dresden), Wolfgang Sommer (Central Institute of Mental Health), Rainer Spanagel (Central Institute of Mental Health), Claudia Speiser (GABO:milliarium mbH & Co. KG), Tade Spranger (Deutsches Referenzzentrum für Ethik / Institut of Science and Ethics), Alicia Stedman (University of Nottingham), Sabina Steiner (Central Institute of Mental Health), Dai Stephens (University of Sussex), Nicole Strache (Charité), Andreas Ströhle (Charité), Maren Struve (Central Institute of Mental Health), Naresh Subramaniam (Cambridge University), Lauren Topper (IoP), Walter (Charité), Robert Whelan (University College Dublin), Steve Williams (IoP), Juliana Yacubian (University of Hamburg), Monica Zilbovicius (INSERM), C Peng Wong (IoP), Steven Lubbe (IoP), Lourdes Martinez-Medina (IoP), Alinda Fernandes (IoP), Amir Tahmasebi (University of Toronto)